Dynamic Real-Time *I–V* Curve Measurement System for Indoor/Outdoor Characterization of Photovoltaic Cells and Modules

Mark D. Yandt, John P. D. Cook, Michael Kelly, Henry Schriemer, *Member, IEEE*, and Karin Hinzer, *Member, IEEE*

***Abstract*—A test method that measures the current-voltage *I–V* curve of a photovoltaic (PV) cell or module in real time is presented as a means of characterizing and understanding the inherently variable nature of performance under field conditions. Temperature, incident light intensity, orientation to the light source, incident spectrum, the uniformity of illumination, as well as a diverse set of failure mechanisms, both catastrophic and otherwise, have characteristic effects on the *I–V* curve. Seeing the *I–V* curve change dynamically with these influences allows visual correlation to real-time events. With a live *I–V* curve generated by performing forward and reversed bias sweeps repeatedly, the effect of parasitic inductance and bias sweep rate on the measurement can be demonstrated directly. This technique also ensures that the device junction is held in quasi-thermal equilibrium during the measurement. The relative alignment of optics in a concentrating photovoltaic module is analyzed to demonstrate the value of the live *I–V* curve.**

***Index Terms*—Bidirectional *I–V* measurement, inductive hysteresis, live *I–V* curve, real time, test station, thermal hysteresis.**

I. Introduction

THE photovoltaic (PV) energy industry is under pressure to provide very inexpensive devices with guaranteed performance over a service life of 20 years or more [1]–[4]. Successful commercial technology innovation and development programs depend on effective understanding and control of all issues contributing to performance, manufacturability, long-term reliability, and lifecycle cost [5]–[10]. Effective electrical characterization of PV cells and modules is critical in order to shorten the associated development cycle [11].

The characteristic current–voltage (*I–V*) curve of a solar cell or module is useful in this regard because it is sensitive to many module design issues, such as spectral response, interconnection problems, optical alignment effects, thermal management issues, bypass diode faults, and parasitic impedances [12], [13].

Manuscript received July 15, 2014; revised September 5, 2014 and October 24, 2014; accepted October 25, 2014. Date of publication November 26, 2014; date of current version December 18, 2014. This work was supported by the Natural Sciences and Engineering Research Council of Canada, the National Research Council of Canada, and the Business Development Bank of Canada.

M. D. Yandt, J. P. D. Cook, H. Schriemer, and K. Hinzer are with Sunlab, University of Ottawa, Ottawa, ON K1N 6N5, Canada (e-mail: markyandt@gmail.com; john.cook@uottawa.ca; hschriemer@uottawa.ca; khinzer@uottawa.ca).

M. Kelly was with the Sunlab, University of Ottawa, Ottawa, ON K1N 6N5, Canada, and is now with Ericsson Canada, Inc., Ottawa, ON K2K 2V6, Canada (e-mail: mkelly09@gmail.com).

Color versions of one or more of the figures in this paper are available online at http://ieeexplore.ieee.org.

Digital Object Identifier 10.1109/JPHOTOV.2014.2366690

TABLE I
TIME SCALE OF PHENOMENA AFFECTING CHARACTERISTIC *I-V* CURVE AND EXAMPLES FROM EACH CATEGORY OF PHENOMENA.

Time Scale	Range	Examples
Very short	$<$ Seconds	Electrical faults, thermal runaway, diode failures [17], [19]
Short	Seconds	Shutter testing [20]
Intermediate	Seconds–hours	Cloud edges, tracker misalignments, associated cell temp. changes [21]
Long	Hours–days	Insolation variation, ambient temperature variation
Very long	Days–years	Soiling [22]–[24], UV damage [25]

Typically, a unidirectional single-scan *I–V* curve measurement is made by driving the module through a voltage range once, while monitoring current output. The initial and final states, as well as the evolution of the device under test (DUT) and its environment during the test, are not necessarily controlled or captured [14], [15]. However, the *I–V* curve is influenced by continually changing temperature, insolation, orientation to the light source, incident spectrum, and uniformity of illumination, as well as a variety of faults.

The time scale of phenomena affecting *I–V* curves can range from very short to very long (see Table I), while conventional *I–V* acquisition times depend on the particular test station design. Any phenomena varying more rapidly than this acquisition time will not be captured with fidelity. Single events affecting *I–V* response will not be captured with a single-scan test system. In field test situations, longer cable bundles are usually necessary between test station and modules, which cause parasitic resistance and inductance effects and require special treatment. In addition, the idle state between each single scan may not be reproducibly controlled, or apparent to the operator. For example, if the idle state is located at $\mathrm{I_{sc}}$, $\mathrm{V_{oc}}$, or $\mathrm{P_{max}}$, the device will equilibrate at corresponding temperatures, which will affect the subsequent *I–V* curves [16]. This complexity suggests that a dynamic display of the real-time *I–V* curve would be valuable when attempting to distinguish among multiple phenomena that change the *I–V* curve at different rates, especially in field operation, since real-time events can be continuously correlated with real-time *I–V* evolution. We propose a test method for continuous rapid display of the *I–V* curve that permits the operator to investigate fast or transient response phenomena and to correlate these with real-time events.

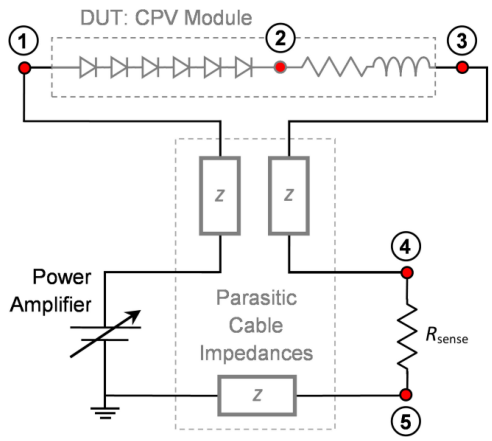

Fig. 1. Schematic of the real time *I–V* test station. The voltage in the bias circuit is measured relative to ground at four points using an oscilloscope in order to achieve two differential measurements and correct for parasitic cable impedances.

II. Experimental System

The test station is intended for both bench and field use to continuously display in real time the characteristic *I–V* curve of the DUT. We use a 200-W four-quadrant dc operational power supply/amplifier (model Kepco 20-10M) with a fast sweep rate (2 V/μs, 0.4 A/μs) to bias the DUT. An external function generator provides a 20 V_{p-p} triangular wave output that feeds the programming input of the Kepco power supply and drives its output voltage through its maximum range of 40 V_{p-p}. A high-speed four-channel digitizing oscilloscope (Agilent Technologies DSO6014A) is employed for the four-point measurements. The DUT is a concentrating PV (CPV) module consisting of six series-connected solar cell receivers each with a bypass diode. It is mounted on a pedestal sun tracker and is connected to the test station by 10-m-long AWG12 cables.

Fig. 1 presents a schematic of the *I–V* test station showing the DUT voltage bias control and five points at which the circuit potential may be monitored. The current through the DUT is determined by a differential voltage measurement from points 4 to 5 across a 0.2-Ω sense resistor R_{sense}. A differential voltage measurement from points 1 to 2 yields the voltage across the DUT. However, if the DUT is packaged in a sealed module then the actual potential difference measured incorporates both the DUT and a short length of cable associated with resistance and inductance as if the differential measurement was made from points 1 to 3.

The four time-dependent voltages V_x measured relative to ground with the oscilloscope are shown in Fig. 2(a). Note that the dashed blue and purple curves have been scaled to more clearly show V_1 and V_5 on the same axis as V_3 and V_4. Note also that the polarities of V_3, V_4, and V_5 have been inverted to comply with convention so that the positive power portion of the resulting *I–V* curve is in the first quadrant, as shown in Fig. 2(b), where the module voltage is given by $V_1 - V_3$, and the module current by $|V_4 - V_5|/R_{sense}$.

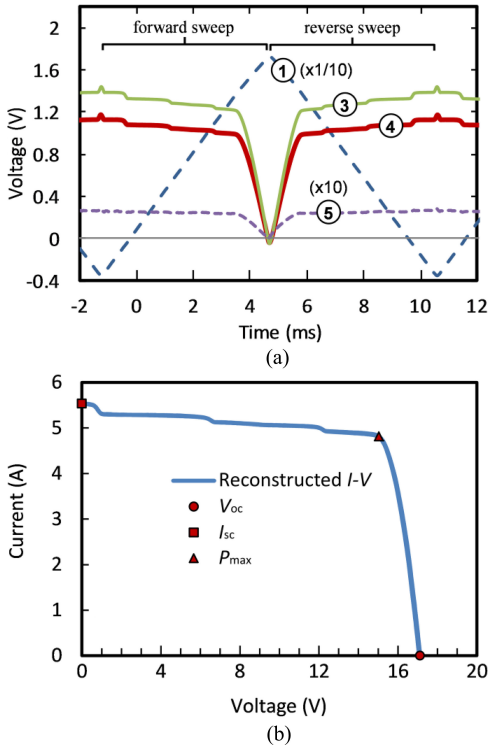

Fig. 2. (a) Time-based measurements made on the four channels of the oscilloscope corresponding to the points indicated in Fig. 1. (b) Reconstructed *I–V* curve with module current $|V_4 - V_5|/R_{sense}$ versus module voltage $V_1 - V_3$. Steps are visible at 0.6, 6.3, and 12.0 V.

The advantage of our approach arises from continuously sweeping the bias across forward and reverse directions. This allows for correlation between the bias sweep rate and any hysteresis in the live measurement. This is important in the field, where long cables are typically required to connect the test station to the PV module and particularly when sense wires for a four-point measurement cannot be placed very close to the DUT because it is sealed inside a module. As discussed below, if the sweep rate is sufficiently high, the DUT is also conveniently held in quasi-thermal equilibrium.

During this discussion, we present data from an alignment study to show the value of visually correlating the real-time adjustment of a particular parameter with its effect on the *I–V* curve. In that investigation, adjustment of module orientation was correlated with the appearance of "steps" in the module *I–V* curve. The added value is not in the instantaneous single scan of the stepped *I–V* curve [see Fig. 2(b)] but rather in the ability to watch how the steps move relative to each other as the module alignment is varied.

Figs. 2(b) and 3 show the reconstructed module *I–V* curve. The steps evident in this particular *I–V* curve are due to mechanical misalignments between the individual optical channels in the module. They are evident because the *I–V* curve was measured during an alignment study for which the module optical axis was adjusted relative to the direct beam, to probe performance at the edge of its acceptance angle. It is challenging to convey in a static figure the intuitive understanding a live *I–V* curve provides as the module alignment is modified. However,

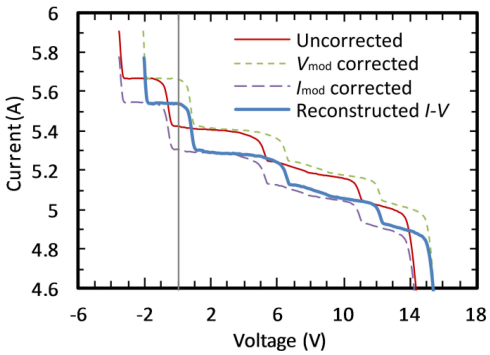

Fig. 3. Effect of parasitic circuit resistances from long cables on module *I–V* measurements. The red uncorrected *I–V* curve includes all series resistance from measurement cables as if it were captured using two-wire measurements of the module voltage and of the current sense resistor voltage. The dashed curves show the implementation of differential measurements around each of these circuit elements independently. The blue curve shows the reconstructed *I–V* curve when differential measurements are implemented for both the module and the sense resistor voltages.

as discussed further in Section III, one can visualize the steps in Fig. 2(b) appearing one at a time out of the dark *I–V* curve as the module comes on-sun, smoothly rising and falling as module alignment is adjusted. Observing the relative movement of steps allows immediate differentiation between different alignment loss phenomena. The resulting insight can be used to improve manufacturing tolerance and performance and to reduce cost.

A. Parasitic Impedance

The effect of the impedance in the connecting wires is mitigated if voltage measurements can be made by connecting directly to the relevant terminals of the DUT and the sense resistor. For field measurements, however, this is often not physically possible, as there are usually built-in module wires whose associated inductances will be in series with the DUT, as exemplified between points 2 and 3 in Fig. 1. Built-in impedances also, in principle, include internal cell capacitance such as that described in [26]–[28], but this is not included in the figure since capacitive effects are negligible in the measurements presented. We distinguish such built-in impedance from the cable impedances shown within the dashed box of Fig. 1 because the effects of the latter can be corrected, while the former cannot.

The *I–V* curves in Fig. 3 show how two differential measurements are used to correct for the voltage drops and phase shifts in the circuit that result from parasitic cable resistances and inductances in the long cables (i.e., the impedances within the dashed box of Fig. 1). The uncorrected curve is what one would measure if the long cables reaching up to the module on the tracker were considered part of the DUT as in a two point measurement, plotting $|V_4|/R_{\rm sense}$ versus $V_1 - V_4$. $I_{\rm mod}$ corrected and $V_{\rm mod}$ corrected show the effects of taking differential measurements around only the sense resistor and only the CPV module, respectively; the thick blue curve includes both of these corrections.

Even though it is not possible to correct the effects of impedances that are *inside* the differential measurements, the fact that the *I–V* curve is swept continuously in both directions means that the effects of these impedances (capacitive or inductive) are immediately apparent in our real-time measurement. Even small inductances of relatively short module wires can cause hysteresis in the *I–V* curve between forward and reverse sweeps when the test station is connected to point 3. This hysteresis occurs at higher bias sweep rates, where the circuit current lags the voltage. This distortion would not be immediately obvious using the single unidirectional scan *I–V* technique, but it is explicitly revealed in the bidirectional continuous display approach, and it can be mitigated by simply reducing the sweep rate, thus ensuring an accurate *I–V* measurement. Note also that a real-time measurement provides a lower bound to the sweep rate because the *I–V* curve must appear live to the eye.

Fig. 4 shows the impact of parasitic impedance on the *I–V* measurements of a single unpackaged triple-junction solar cell on a receiver. The *I–V* curves for bias sweep rates from 690 to 6900 V/s were measured under controlled laboratory conditions using a Spectrolab XT-30 high-concentration solar simulator with continuous illumination. Fig. 4(a) shows the measurement results when the sense wires are connected to point 3, as an AWG12 cable provides a small series impedance between points 2 and 3. Fig. 4(c) shows the results for a direct connection of the sense wires to point 2, which is possible in this case because the cell is not protected within a module. The hysteresis seen in the former, primarily due to cable inductance, exists for sweep frequencies greater than 690 V/s. By contrast, no hysteresis is seen in the latter case, as the direct connection has minimal inductance. Capacitive reactance would be observed as voltage lagging current, but we observe the opposite, since inductive reactance dominates as shown in Fig. 4(a).

SPICE simulations of the circuit in Fig. 1 were compared with the measurement results to see if the impedances could be reconstructed. The simulated AWG12 results are shown in Fig. 4(b) for comparison with the measurements of Fig. 4(a). The $R = 20$ mΩ resistance value found is in general agreement with the sum of typical contact ($\sim$5 mΩ per contact) and line resistances (5.2 mΩ/m). The $L = 2$ μH inductance value found is in reasonable agreement with the expected 2.7-μH wire inductance calculated using [29]:

$$L = 2l\left[\ln\left(4l/d\right) - 1 + \frac{\mu}{4} + \frac{d}{2l}\right] \tag{1}$$

where L is in μH, $l = 200$ cm is the wire length, $d = 0.2053$ cm is its diameter, and $\mu = 1$ is the wire's relative magnetic permeability. Likewise, simulations of a direct connection, as shown in Fig. 4(d) using $L = R = 0$, are in agreement with the measured results shown in Fig. 4(c).

B. Effective Junction Temperature

In the single-scan test method, the temperature of the cell-carrier assembly assumes the value dictated by the idle condition of the test station. By contrast, in our dynamic approach, the test station is continuously changing the bias point; therefore, the temperature of the DUT is dictated by the evolution of the power extracted from the cell during repeated sweeps. At low sweep

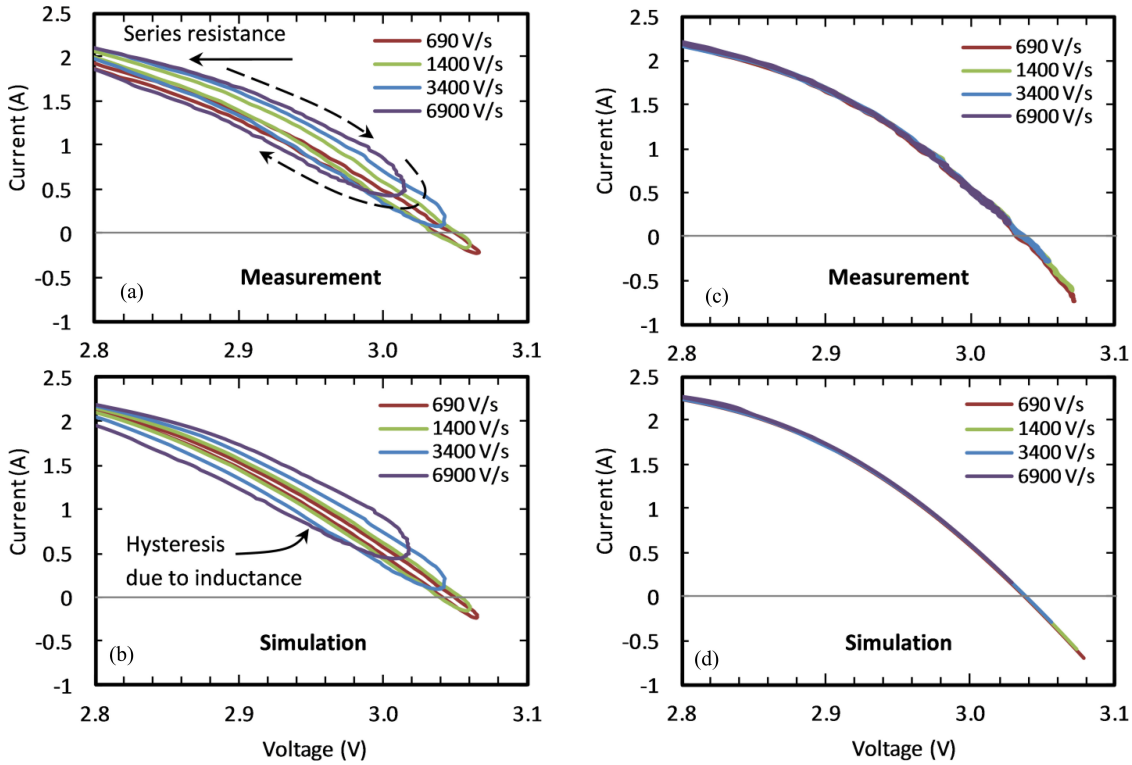

Fig. 4. (a) Measured and (b) simulated *I–V* curves of a triple-junction cell measured at sweep rates between 690–6900 V/s for which the connection between points 2 and 3 was a 200-cm AWG 12 cable. Dashed arrows indicate sweep direction confirming an inductive effect in which the current lags the voltage. (c) Measured and (d) simulated *I–V* curves of a triple-junction cell measured at sweep rates between 690–6900 V/s for a direct connection to point 2.

rates (<500 V/s), small inductances between points 2 and 3 have no significant impact on the cell's *I–V* characteristic, as demonstrated in Fig. 5. However, hysteresis is visible at a bias sweep rate of 0.69 V/s since the cell-carrier assembly's thermal time constant is similar to the sweep rate. At lower sweep rates (<1 V/s in this case, a rate which is dependent on thermal coupling to the heat sink beneath the cell), the temperature of the cell begins to follow bias point changes, with individual *I–V* points recorded at different cell junction temperatures. At higher sweep rates, the junction temperature does not have sufficient time to change before the bias point has scanned through the entire *I–V* curve; thus, quasi-thermal equilibrium is reached.

The average power extracted from the solar cell during testing at any sweep rate can be calculated from the time-weighted average of the power curve within the range of the voltage sweep as explained in [16]. If desired, this can be used to adjust the maximum power point (MPP) to the thermal conditions that prevail during static operation. It is also noteworthy that the solar cell is held at a temperature much closer to its MPP temperature so that the magnitude of the correction required is small compared with that required when a solar cell is idled at open-circuit voltage or at short-circuit current.

III. Applications

The characterization study described previously provides the basis for dynamic display and capture of accurate *I–V* curves over long cable bundles in the field, with proper understanding of reactive parasitics and junction temperature dynamics. Almost all testing applications benefit from such capability, but a few are of particular interest.

The ability to capture and even resolve the dynamics of an operational change or component failure that occurs during a stress test is useful and is a capability that is not easily achieved by other means. Traditional methods (i.e., taking instantaneous *I–V* scans or monitoring a single bias point over time) do not provide a complete time-resolved picture of the *I–V* curve. Live *I–V* capability allows for very short and intermediate length single events that can change any part of the *I–V* curve to be correlated in time with external influences on the cell.

Examples of tests that have the potential to change the *I–V* curve or to cause cell failures include: mechanically bending the module (very short to short time scale), mechanically bending the concentrating optics (very short to short), partially shading cells or groups of cells in strings (short) [11], heating or cooling a cell assembly (intermediate) [30], and moving the module off axis or through the edge of its acceptance angle (intermediate) [31]. It is also possible to resolve and visualize the performance penalty paid when a tracking system updates its pointing direction in discrete coarse steps rather than in a continuous fashion (short to intermediate) [32].

To demonstrate the value of the live *I–V* curve, we expand our explanation of the alignment study first presented in Fig. 2. The "staircase" *I–V* curves in Fig. 2(b) are a result of differences in the distinct *I–V* characteristics of the six individual channels (cell receiver and optics) that comprise the module

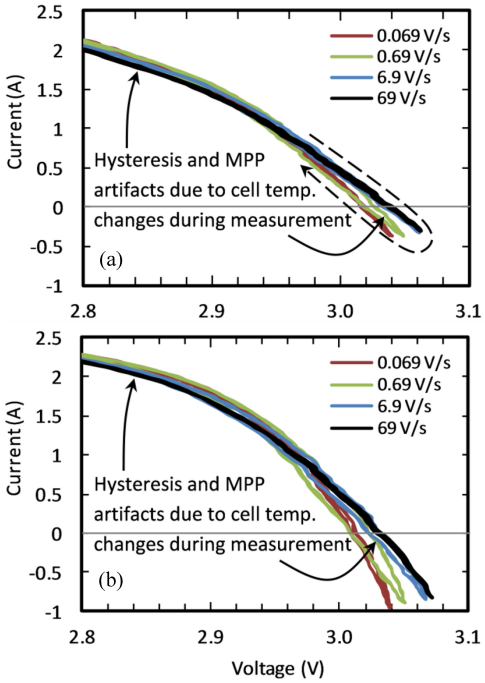

Fig. 5. *I–V* curves of a triple-junction cell measured at sweep rates between 0.069–69 V/s bounding the cell-carrier thermal time constant with (a) connection to point 3 with a 1.2-m AWG 12 cable between points 2 and 3 and (b) direct connection to point 2. Dashed arrow indicates sweep direction. The red curve shows the result of an extremely slow sweep rate in which the MPP and the V_{oc} are increased and decreased, respectively, due to different levels of electrical power extraction (and, hence, cell temperature) during different parts of the measurement.

response. Since this is a CPV module, the concentrating optics must be aligned along their direct normal axis. Differing deviations of individual optical axes from direct normal mean that these acceptance angles are not all mutually coincident. This is confirmed by an alignment study, where the sun is deliberately allowed to walk through the acceptance angle of the module. As the direct beam begins to enter the acceptance angle of the most negatively aligned optic, its light *I–V* curve begins to rise out of the module dark *I–V* curve in real time. As the module comes more fully on sun, *I–V* curves from the other cells begin to contribute. The number of steps in the *I–V* curve changes depending on the number of channels that are adequately aligned. This staircase effect is minimized when the module alignment is optimal. The real acceptance angle can be measured directly by watching the live picture of the *I–V* curve as the module is misaligned relative to any direct beam either on sun or in the lab. Fig. 6 shows a series of snapshots taken every 30 s, while the live *I–V* curve was evolving on screen. It shows that the steps are not evenly spaced in current and that their relative spacing is changing as the module moves off sun. This confirms that the type of misalignment is not the same from one optical channel to the next. The live aspect of the curve is critical because it shows the viewer how fast each step is rising/falling relative to the others indicating the nature of the misalignments. It allows the operator to adjust individual channels (e.g., push on bowing lenses, or twist the whole module) to determine the role (i.e., the

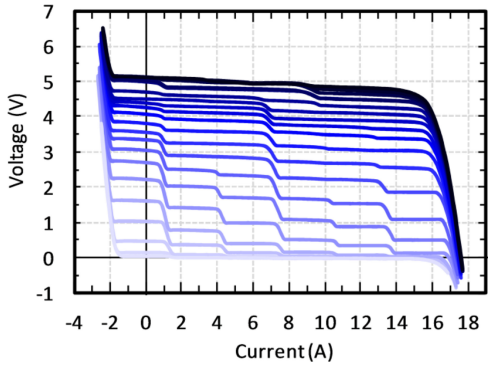

Fig. 6. Snapshots taken as the sun moved off the optical axis of a six-cell CPV module. Tracker alignment was manually frozen, while the live *I–V* characteristics were monitored. The *I–V* curves are shown for module alignments 0° (top) through 2.7° off axis (bottom) in 0.14° increments.

on-screen effect on the module *I–V* curve) that various factors are playing on the optical alignment.

IV. Conclusion

A test station has been presented that permits continuous display of the real-time characteristic *I–V* curve of a solar cell or module. The time evolution of the *I–V* curve resolves the module response to internal and external real-time events. For example, rapid changes arising from electrical intermittencies and component overstress failure can be distinguished from slower component degradation and insolation effects.

The proposed test station also ensures that unknown idle state effects do not arise, since a sufficiently rapid bidirectional scan holds the PV device in a quasi-thermal equilibrium. The value of the bidirectional scan is highlighted and temperature and inductance related hysteresis in the *I–V* curve is characterized, where hysteresis phenomena are already known and characterized in established PV technologies, the optimal scan rate has been previously established, and a single-scan capture is safe. The bidirectional dynamic display addresses the more general situation in new technologies or field installations, where a hysteresis may be operating but is unknown to the test engineer. Inductive parasitic artifacts are quickly and easily recognized in this noninvasive method and can be mitigated by optimizing the sweep rate before recording an *I–V* response. This method has been demonstrated at scan rates from 0.069 through 6900 V/s. With appropriate instrumentation, the method could be extended further to phenomena that are too slow or too fast for the human eye, including, in principle, flash testing.

Acknowledgment

The authors would like to thank F. Szadkowski, M. Armstrong, and M. Swinton of the Canadian Centre for Housing Technology at Natural Resources Canada for scientific and field support.

REFERENCES

[1] J. E. Haysom, O. Jafarieh, H. Anis, and K. Hinzer, "Concentrated photovoltaics system costs and learning curve analysis," *AIP Conf. Proc.*, vol. 1556, pp. 239–243, 2013.

[2] S. Kurtz, "Opportunities and challenges for development of a mature concentrating photovoltaic power industry," Nat. Renewable Energy Lab., Golden, CO, USA, Tech. Rep., NREL(TP-520–43208 1556, 2013.

[3] D. J. Friedman, R. R. King, R. M. Swanson, J. McJannet, and D. Gwinner, "Editorial: Toward 100 gigawatts of concentrator photovoltaics by 2030," *IEEE J. Photovoltaics*, vol. 3, no. 4, pp. 1460–1463, Oct. 2013.

[4] K. Brankera, M. J. M. Pathaka, and J. M. Pearce, "A review of solar photovoltaic levelized cost of electricity," *Renewable Sustainable Energy Rev.*, vol. 15, no. 9, pp. 4470–4482, 2011.

[5] V. M. Fthenakis and H. C. Kim, "Photovoltaics: Life-cycle analyses," *Sol. Energy*, vol. 85, no. 8, pp. 1609–1628, 2011.

[6] W. E. Deming, *Out of Crisis*. Cambridge, MA, USA: MIT Press, 2000.

[7] J. M. Juran, *Juran on Planning for Quality*. New York, NY, USA: Collier-Macmillan, 1993.

[8] A. F. Sherwani, J. A. Usmani, and Varun, "Life cycle assessment of solar PV based electricity generation systems: A review," *Renewable Sustainable Energy Rev.*, vol. 14, no. 1, pp. 540–544, 2010.

[9] J. H. Wohlgemuth, D. W. Cunningham, P. Monus, J. Miller, and A. Nguyen, "Long term reliability of photovoltaic modules," in *Proc. IEEE 4th World Conf. Photovoltaic Energy Convers.*, May 2006, pp. 2050–2053.

[10] S. Kurtz, J. Granatab, and M. Quintana, "Photovoltaic-reliability R&D toward a solar-powered world," *Proc. SPIE*, vol. 7412, pp. 1–12, Aug. 2009.

[11] F. J. Vorster and E. E. van Dyk, "Current-voltage characteristics of high-concentration, photovoltaic arrays," *Prog. Photovoltaics: Res. Appl.*, vol. 13, no. 1, pp. 55–66, 2005.

[12] K. Emery, "Measurement and characterization of solar cells and modules," in *Handbook of Photovoltaic Science and Engineering*. New York, NY, USA: Wiley, 2003.

[13] C. R. Osterwald, "Standards, calibration and testing of PV modules and solar cells," in *Practical Handbook of Photovoltaics: Fundamentals and Applications*. New York, NY, USA: Elsevier, 2003.

[14] E. Duran, M. Piliougine, M. Sidrach-de-Cardona, J. Galan, and J. M. Andujar, "Different methods to obtain the I-V curve of PV modules: A review," in *Proc. 33rd IEEE Photovoltaic Spec. Conf.*, May 2008, pp. 1–6.

[15] M. Piliougine, J. Carretero, L. Mora-López, and M. Sidrach-de-Cardona, "Experimental system for current voltage curve measurement of photovoltaic modules under outdoor conditions," *Prog. Photovoltaics: Res. Appl.*, vol. 19, no. 5, pp. 591–602, 2011.

[16] M. D. Yandt, J. F. Wheeldon, J. P. D. Cook, R. Beal, A. W. Walker, O. Thériault, H. Schriemer, T. J. Hall, and K. Hinzer, "Estimating cell temperature in a concentrating photovoltaic system," *AIP Conf. Proc.*, vol. 1477, pp. 172–175, 2012.

[17] C. G. Zimmermann, "Thermal runaway in multijunction solar cells," *Appl. Phys. Lett.*, vol. 102, no. 23, pp. 233506-1–233506-4, 2013.

[18] N. G. Dherea, N. Shiradkara, E. Schnellera, and V. Gade, "The reliability of bypass diodes in PV modules," *Proc. SPIE*, vol. 88250I, pp. 1–8, Aug. 2013.

[19] M. Steiner, G. Siefer, and A. W. Bett, "Modeling the thermal runaway effect in CPV modules," *AIP Conf. Proc.*, vol. 1556, pp. 230–233, 2013.

[20] J. P. D. Cook, M. D. Yandt, M. Kelly, J. F. Wheeldon, K. Hinzer, and H. Schriemer, "Shutter array technique for real-time non-invasive extraction of individual channel responses in multi-channel CPV modules," *Proc. SPIE*, vol. 8915, pp. 891509-1–891509-8, Jun. 2013.

[21] N. Bosco, T. J. Silverman, and S. Kurtz, "Modeling thermal fatigue in CPV cell assemblies," *IEEE J. Photovoltaics*, vol. 1, no. 2, pp. 242–247, Oct. 2011.

[22] M. Vivar, R. Herrero, I. Antón, F. Martínez-Moreno, R. Moretón, G. Sala, A. W. Blakers, and J. Smeltink, "Effect of soiling in CPV systems," *Sol. Energy*, vol. 84, no. 7, pp. 1327–1335, 2010.

[23] A. Massi Pavan, A. Mellit, and D. De Pieri, "The effect of soiling on energy production for large-scale photovoltaic plants," *Sol. Energy*, vol. 85, no. 5, pp. 1128–1136, 2011.

[24] M. García, L. Marroyo, E. Lorenzo, and M. Pérez, "Soiling and other optical losses in solar-tracking PV plants in Navarra," *Prog. Photovoltaic: Res. Appl.*, vol. 19, no. 2, pp. 211–217, 2011.

[25] E. L. Meyer and E. E. van Dyk, "Assessing the reliability and degradation of photovoltaic module performance parameters," *IEEE Trans. Reliab.*, vol. 53, no. 1, pp. 83–92, Mar. 2004.

[26] Y. Hishikawa, H. Shimura, and H. Tobita, "Accurate I-V curve measurements of high-capacity c-si solar cells: Effects of I-V testers and new technology for rapid measurement," in *Proc. 28th Eur. Photovoltaic Sol. Energy Conf.*, 2013, pp. 3159–3161.

[27] C. Monokroussos, R. Gottschalg, A. N. Tiwari, G. Friesen, D. Chianese, and S. Mau, "The effects of solar cell capacitance on calibration accuracy when using a flash simulator," in *Proc. IEEE Photovoltaic Energy Convers.*, 2006, pp. 2231–2234.

[28] T. Chayavanich, C. Limsakul, N. Chayavanich, D. Chenvidhya, C. Jivacate, and K. Kirtikara, "Describing dynamic behavior of static IV characteristics of PV modules using dynamic impedance," in *Proc. 21st Eur. Photovoltaic Sol. Energy Conf.*, Sep. 2006, pp. 2464–2465.

[29] F. W. Grover, *Inductance Calculations*. New York, NY, USA: Dover, 2004.

[30] A. B. Maish, "PV concentrator array field performance measurement," *Sol. Cells*, vol. 18, no. 3–4, pp. 363–371, 1986.

[31] H. Mousazadeha, A. Keyhani, A. Javadi, H. Mobli, K. Abriniac, and A. Sharib, "A review of principle and sun-tracking methods for maximizing solar systems output," *Renewable Sustainable Energy Rev.*, vol. 13, no. 8, pp. 1800–1818, 2009.

[32] C. Algora, "Reliability of III–V concentrator solar cells," *Microelectron. Reliab.*, vol. 50, no. 9–11, pp. 1193–1198, 2010.

Mark D. Yandt received the B.Eng.Mgt. degree in engineering physics and management from McMaster University, Hamilton, ON, Canada, and the M.A.Sc. degree in electrical and computer engineering from the University of Ottawa, Ottawa, ON, and is currently working toward the Ph.D. degree with the School of Electrical Engineering and Computer Science, University of Ottawa, studying under K. Hinzer and H. Schriemer.

His research interests include the development, characterization, optimization, and deployment of photovoltaic and concentrating photovoltaic systems. He oversees experimental design and system characterization for a number of projects at the Sunlab that involve the dynamics and reliability of high-concentration photovoltaic systems.

Mr. Yandt received an Ontario Graduate Scholarship (OGS) in 2011 and the Alexander Graham Bell Canada Graduate Scholarship (CGS-D) funded by the Natural Sciences and Engineering Research Council of Canada in 2012.

John P. D. Cook received the B.Sc. degree in chemistry from McGill University, Montreal, QC, Canada, and the Ph.D. degree from the University of British Columbia, Vancouver, BC, Canada, supported by the Killam Predoctoral Scholarship.

He received a Natural Sciences and Engineering Research Council of Canada Overseas Postdoctoral Fellowship to continue studies in electron spectroscopy at the Flinders University of South Australia (1981–1983), achieving the first binary (e, 2e) results on free radical and relativistic molecular targets. He joined Bell-Northern Research in 1984 and began work on characterizing III–V compound semiconductor optoelectronic materials and devices with the Advanced Technology Laboratory, later moving into wafer process development and reliability studies for optical fiber access devices at Nortel Networks, including high-speed photodiodes, integrated laser/back-facet-monitor devices, and high-speed electronics, in scientist and manager roles. In 2006, he began concentrator photovoltaic module development in private industry, and in 2010, he joined Sunlab, the University of Ottawa, Ottawa, ON, Canada, as a Research Associate. His recent work has been supported by the National Science and Engineering Research Council of Canada, Ontario Centers of Excellence, the University of Ottawa, and several industrial partners.

Michael Kelly received the B.A.Sc. degree in electrical engineering from the University of Ottawa, Ottawa, ON, Canada.

He is currently an RF Hardware Engineer at Ericsson Canada, Inc., where he works in the wireless communication department. He had a summer position with the Sunlab in 2013, where he worked closely with M. Yandt on the modeling of electric-circuit parasitic dynamics during the characterization of high-efficiency photovoltaic systems. He went on to complete an award winning undergraduate project in partnership with the Sunlab in which he developed a new test station capable of probing internal cell dynamics.

Henry Schriemer (M'00) received the B.Sc. degree in mathematics and the Ph.D. degree in physics from the University of Manitoba, Winnipeg, MB, Canada, in 1987 and 1997, respectively.

He is currently an Associate Professor of electrical engineering with the University of Ottawa, Ottawa, ON, Canada, where he previously held an NCIT Research Fellowship in photonics from 2003 to 2005. His research interests include engineered complex systems, with a focus on photonic technologies for energy efficiency. His current activities range from the modeling of multijunction concentrator solar cells and systems, reliability studies and accelerated aging, the development of spectral models that incorporate local weather conditions, and the impact of variable generation on the electrical distribution system. Prior to this, he spent several years in the photonics industry, where he is recognized as one of the innovators of strain-engineered planar lightwave circuits. His previous research accomplishments have ranged from the description of optical singularities in photonic crystals to fundamental advances in the design and realization of laterally coupled-distributed feedback lasers. He has authored more than 70 refereed publications. He held a Postdoctoral Fellowship in laser physics and nanophotonics with the Van der Waals-Zeeman Institute, Amsterdam, The Netherlands, where he made the first measurements of significant spontaneous emission inhibition in active photonic crystals.

Karin Hinzer (M'08) received the B.Sc., M.Sc., and Ph.D. degrees in physics from the University of Ottawa, Ottawa, ON, Canada, in 1996, 1998, and 2002, respectively.

She is currently an Associate Professor and the Canada Research Chair in photonic nanostructures and integrated devices and an Associate Professor with the School of Electrical Engineering and Computer Science, University of Ottawa. She has made pioneering contributions to the experimental physics of quantum dots marked by two landmark papers in *Science*. She gained extensive experience in the design and fabrication of group III-V semiconductor devices while with the National Research Council Canada, Nortel Networks, and Bookham. Cost-reduction strategies and liaison with remote fabrication facilities strongly feature in her industry experience. She joined the University of Ottawa in 2007, where she is the founder of the Sunlab, which is a modeling and characterization laboratory specializing in the development of high-efficiency solar cells. Since the laboratory's inception, she has trained more than 80 highly qualified personnel in the field of photovoltaic system and devices. Since 2010, she has been with the Inorganic Photovoltaics Cotheme Leader within the Pan-Canadian Photovoltaic Research Network.

Dr. Hinzer received the Inaugural Canadian Energy Award, with industry partner Morgan Solar, for the development of more efficient solar panels, in 2010.